

$H\alpha/H\beta$ a Galactic Low Energy Cosmic Rays tracer

I. Busa¹, S. Cabibbo^{1,2}, C. Trigilio¹, and F. Leone^{1,2}

¹ INAF, Osservatorio Astrofisico di Catania, Via S. Sofia 78, I-95123 Catania, Italy

² Dipartimento di Fisica e Astronomia, Sezione Astrofisica, Università di Catania, Via S. Sofia 78, I-95123 Catania, Italy

Received ; accepted

ABSTRACT

Context. Investigating the diagnostic power of $H\alpha/H\beta$ Charge-Exchange (CE) emission as Low-Energy Galactic Cosmic Rays (LECRs) tracer in diffuse regions.

Aims. In this work, we define and test a spectroscopic indicator of CE reactions between LECRs protons and neutral hydrogen atoms of the diffuse medium. This indicator can be used for mapping LECRs density in diffuse clouds and can lead to the identification of new LECRs sources as we expect density variations caused by the distance between an observed cloud and the nearest site of particle acceleration. We also lay the foundations for the definition of a photometric indicator to be used in the next full-sky photometric surveys such as the Vera Rubin 10-year Legacy Survey of Space and Time (LSST).

Methods. Based on literature cross-sections, we calculate $H\alpha/H\beta$ line profile ratio in the case of CE emission and compare it with the recombination process ratio in order to define a CE indicator. We then test our results on the Balmer-dominated filaments of the supernova remnant RCW 86 and we explore how the spectroscopic constraints can turn into a photometric indicator based on colour indices.

Results. We find that, in shocked environments, CE between LECRs and neutral hydrogen become the dominant process for Balmer lines emission. The hydrogen spectroscopic emission is expected to be modified, with respect to the recombination Balmer decrement, to result in double the $H\alpha/H\beta$ with respect to a similar but quiescent region. The test on the known Balmer-dominated filaments of the supernova remnant RCW 86 confirm the efficiency of our spectroscopic indicator. Therefore we explore possible conversions of the spectroscopic indicator into colour indices combinations. This is the first step toward the definition and test of a photometric indicator for tracing LECRs to be applied in the LSST pipelines to photometrically identify new LECRs accelerators in the whole Galaxy.

Key words. Cosmic Rays: acceleration of charged particles - Balmer emission – ISM: supernova remnants – Methods: photometry - charge-exchange - color indexes

1. Introduction

Low-energy cosmic rays (LECRs), charged particles with < 100 MeV energies, play a fundamental role in the physics and evolution of our Galaxy. LECRs, unlike ionizing radiation, can penetrate large column densities of gas, and maintain there a gas ionization fraction that allows the coupling between the plasma and the magnetic field, which in turn affects the dynamical evolution of clouds and impacts on the process of star and planet formation. The ionization rate measured in molecular clouds results to be higher than the predicted from supernova remnants (SNRs), suggesting that LECRs could not have the same origin as higher energy cosmic rays (Gabici 2022). Furthermore, in the last few years more and more authors assert, based on both theoretical and experimental pieces of evidence, that, in addition to the well-established SNRs sources, more sources should contribute to the flux of cosmic rays (CRs), especially at low energy. Observations of the heliosphere, in fact, indicate magnetic reconnection as a possible galactic CRs accelerator. Furthermore, composition measurements by ACE (Stone et al. 1998) and TIGER (Rauch et al. 2009) showed that CRs source abundances are consistent with a mixture of about 80% of the material with primordial solar composition and the remaining 20% of the material enriched by stellar outflows and ejecta (Murphy et al. 2016). Another evidence is the overabundance of roughly a factor of 5 of ^{22}Ne with respect to expectations (Tatischeff et al. 2021), which suggests

that a significant fraction of galactic CRs is accelerated out of Wolf-Rayet wind material, enriched in helium-burning products. Finally, the recent detection of ^{60}Fe in CRs with a half-life of about 2.6 Myr allows setting an upper limit of a few million years on time between nucleosynthesis of these nuclei and detection at Earth, as is the case if a local association of OB stars injected them. These are only some of the evidence that led to the conclusion that SNRs cannot be the only accelerating source of CRs in our Galaxy. For a more in-depth critical review of these and other important clues, please refer to the recent paper of Gabici et al. (2019). All these exciting discoveries have paved the way for other new possible galactic accelerators candidates, such as Wolf-Rayet (WR), Luminous Blue Variable (LBV), Flare, and Chemically Peculiar (mCP) stars.

Considering all these factors, it is evident how the measure of CRs distribution in our Galaxy is of utmost importance. Measuring CRs can be achieved through two very different types of methods, which we can refer to as 'local measurements' (near-Earth) and 'remote measurements' (at some given location in the Galactic disk). In the former type, CRs are measured through the electromagnetic cascade they produce by interacting with the particles of the Earth's atmosphere. This approach is based upon a detailed theory on the particles' acceleration and their transport up to the Earth. Consequently, it requires hypotheses on the properties of the acceleration and on the characteristics of the

medium (magnetic field, turbulence, etc.), which are uncertain and often arbitrary. Furthermore, whereas high-energy CRs can penetrate the inner heliosphere reaching the Earth almost undisturbed, LECRs must overcome the solar wind which strongly affects and modulates the measurements of the CRs spectrum on the Earth. For this reason, conclusive evidence for the effective acceleration of LECRs from sources other than SNRs is expected to be provided by the second method, based on the detection of electromagnetic waves whose transport, unlike for charged particles, is not affected by galactic, solar, and terrestrial magnetic fields. Different mechanisms contribute to the CRs emission in the different portions of the electromagnetic spectrum. Radio emission primarily occurs through the process of synchrotron radiation, that is the emission of photons by charged CRs (typically electrons) accelerating or decelerating in strong magnetic fields. Observationally, synchrotron radiation is detected across a wide range of astrophysical objects, such as pulsars, gamma-ray bursts (GRBs), active galactic nuclei (AGN), and the already mentioned SNRs. The energy of the emitted photons involves not only the radio wavelengths (sub-millimetre to meter range) but it may extend also up to the X-ray energies (keV to MeV range). X-ray emission occurs also through bremsstrahlung from high-energy CRs being deflected by the electromagnetic field of the atomic nuclei and electrons of the medium. The energetics of X-ray emission can vary widely depending on the characteristics of the cosmic ray and the material it interacts with. CRs with energies in the range of several GeV to PeV can generate X-rays with energies in the range of keV-MeV, even though lower-energy CRs can also produce photons in the soft X-ray range. Observation examples of X-ray emission include SNRs, AGNs, Pulsar Wind Nebulae (PWNe), high-mass X-ray binaries and many others. At higher frequencies, gamma-ray emission, spanning a wide range of energy from a few MeV to several TeV, primarily occurs through two mechanisms: hadronic and leptonic processes. The former involves the interactions of high-energy CRs, typically protons or heavier nuclei, with atomic nuclei in the matter. These interactions can result in the production of neutral and charged pions which subsequently decay, releasing gamma-ray photons. Leptonic processes involve the interactions of high-energy CRs, typically electrons or positrons, with matter or electromagnetic fields through mechanisms such as inverse Compton scattering or the decay of high-energy electrons and positrons. Gamma-ray emission has been detected in numerous astrophysical sources too, including GRBs, AGN, and SNRs.

All the portions of the electromagnetic spectrum discussed overhead have been the most investigated thus far. Nonetheless, the optical counterpart has also recently been gaining considerable importance. A more in-depth exploration of this particular aspect of the CRs acceleration issue would be extremely useful, especially in anticipation of the new great optical surveys which will start in the near future, such as the Vera C. Rubin 10-year *Legacy Survey of Space and Time* (LSST) (Ivezic et al. 2019). In order to further investigate this research field, one of the potential avenues to be explored, which is addressed in this article, is the emission produced by the process of interaction of Charge Exchange (CE) between LECRs and neutral hydrogen as LECRs indicator in the diffuse medium. Indeed, it is well known that the non-thermal $H\alpha$ enhancement observed in the non-radiative filaments usually present at the edge of SNRs is a powerful diagnostic of CRs accelerators' efficiency since it is commonly understood in terms of CE processes between the shock-accelerated protons of the SNRs and the slow neutral hydrogen of the interstellar medium (ISM). The understanding of these emission mechanisms is mostly based on the seminal paper

of Chevalier et al. (1980) and a critical review that summarizes the state of theory and observations of this research field can be found in the paper by Heng (2010, and references therein). The basic idea behind these researches is that the CE reactions add a broad component to the narrow $H\alpha$ emission line, from whose spectral profile we can infer some fundamental properties of the underlying shock. In more recent work, Morlino et al. (2012) show how the significance of the different emission line components is substantially related to three important parameters: the fraction of ionised hydrogen, the electron-ion temperature equilibration and the shock velocity. Morlino and coworkers considered a plasma with a numerical density of $n = 0.1 \text{ cm}^{-3}$ and an ionization fraction of 0.5 and showed that the full-width at half-maximum (FWHM) of the broad component of the $H\alpha$ emission depends on the shock velocity as well as on the electron-ion equilibration level, taken into account through the two parameters β_{up} and β_{down} , which refer respectively to the upstream and downstream of the shock. Another important observable very often considered in this kind of research is the ratio of the broad to narrow component of the $H\alpha$ emission line, which, analogously to the previous case, is a function of the shock velocity and also depends on the temperature equilibration level of the electrons respect to the protons. The same emission mechanism described above can be expected to be observed in the diffuse clouds present around the other possible galactic CRs accelerator candidates and the purpose of this work is to identify a method to check the presence of this emission mechanism around all possible galactic CRs accelerator candidates. In order to achieve this goal, we define a spectroscopic indicator for CE between $\sim \text{MeV}$ protons and neutral hydrogen based on the theoretical/observational study of the $H\alpha/H\beta$ ratio and we test our spectroscopic indicator on the Balmer-dominated filaments of the supernova remnant RCW 86. With spectroscopic surveys at a high spatial and temporal resolution of the diffuse medium still out of our reach, such a spectroscopic indicator is not immediately usable. On the other hand, a CE photometric indicator would be fundamental in view of the optical photometric surveys of the next decade, such as the already mentioned *Legacy Survey of Space and Time* mission of the Vera C. Rubin Observatory, for mapping LECRs density in the Galaxy, giving clues to their origin and distribution. With the aim of obtaining a CE photometric indicator, we explore possible conversions of the spectroscopic indicator into colour indices combinations and analyse their efficiency as CE indicators on simulated images of the Rubin telescope.

2. Mathematical derivations of Charge-Exchange contribution to $H\alpha / H\beta$

2.1. $H\alpha$ and $H\beta$ line formation

As shown in the Grotrian diagram of Fig. 1, the Balmer $H\alpha$ line results from the hydrogen deexcitation from level 3s and 3d to 2p as well as from 3p to 2s (red lines). The latter case is complicated by the fact that the 3p level can also decay into 1s, producing Ly β photons. Depending on the optical depth of the medium, these photons can either escape the system or be reabsorbed by ground-state hydrogen and eventually reemitted as $H\alpha$ photons. In the literature, two limit cases are generally considered. Case A refers to the assumption that the emitting region is optically thin in all H I emission lines and case B to the assumption that the emitting region is optically thick in the Lyman lines. To take into account the two different scenarios, we can use the branching ratio $B_{u,d}$, which is the fraction of transitions $u - d$ with re-

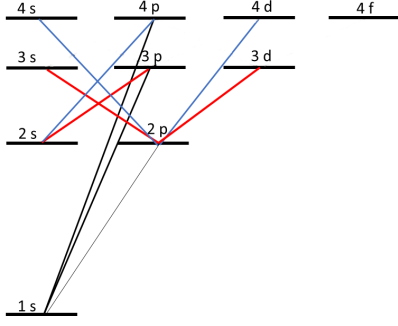


Fig. 1. Grotrian diagram of involved levels in the Balmer H α (in red) and H β (in blue) line formation.

| Branching ratio | Case A | Case B |
|-----------------|--------|--------|
| $B_{3p,2s}$ | 0.1183 | 1 |
| $B_{4s,2p}$ | 0.5841 | 1 |
| $B_{4d,2p}$ | 0.7456 | 1 |
| $B_{4p,2s}$ | 0.1190 | 1 |

Table 1. Relevant branching ratio for the H α and H β transition, in the case A and B (see text).

spect to the total. In the case B, the branching ratio is ~ 1 (all Lyman photons are converted to Balmer or subsequent spectral series). In the case A, the branching ratio is simply obtained by the Einstein A-coefficient for a given transition $A_{u,d}$ (where the subscript u, d refer to the upper and lower level of the radiative transition) normalized by the Einstein A-coefficients of all of the transitions allowed by the electric dipole selection rule.

$$B_{u,d} = \begin{cases} A_{ud} / \sum_i A_{ui} & \text{Case A} \\ 1 & \text{Case B} \end{cases}$$

In the particular case of H α , for example, the branching ratio $B_{3p,2s}$ is equal to 1 in the case B (all Ly β photons are converted to H α). In the case A, using values from the NIST Atomic Spectra Database (Kramida et al. 2021) list in Tab. A.1 of Appendix A we obtain

$$B_{3p,2s} = A_{3p,2s} / (A_{3p,2s} + A_{3p,1s}) = 0.1183$$

Referring to the Grotrian diagram of Fig. 1, the Balmer H β line results from the hydrogen deexcitation from level 4s and 4d to 2p as well as from 4p to 2s (blue lines). Once again, the latter case is complicated by the fact that the 4p level can also decay into 1s, producing Ly γ photons, or in 3s or 3d, producing Pa α photons. In the same way, level 4s and 4d can decay into 3p, producing again Pa α photons. As for the H α transition, we can define the relevant branching ratios for the H β line formation, $B_{4s,2p}$, $B_{4p,2s}$ and $B_{4d,2p}$, that in the case B, we can assume to be unitary, since they are at least an order of magnitude greater than the corresponding relevant branching ratios for the Pa α transition: $B_{4p,3s}$, $B_{4p,3d}$, $B_{4s,3p}$ and $B_{4d,3p}$. All necessary branching ratios for the H α and H β transition, in the case A and B, are summarized in Tab. 1.

2.2. H α and H β line formation in astrophysical shocks

Fast, astrophysical shocks are examples where collisional excitation becomes important. In particular, a class of shocks known as *Balmer-dominated shocks* (BDSs) are believed to be driven by astrophysical pistons (e.g. supernova remnants, pulsar wind nebulae, novae) impinging upon the ambient interstellar medium, so

that both the processes, excitation and CE are inferred to be at work Chevalier & Raymond (1978). The theory of Balmer line formation in the presence of shocks was developed essentially for interpreting observational data in Balmer-dominated filaments of SNRs, structures of hot, expanding plasma shells, resulting from the interaction of supernova ejecta with circum and interstellar matter. SNRs are generally very extended sources ($>1'$ in the Milky Way) and have a roughly spherical shell shape sometimes surrounded by small, faint filaments in expansion with optical emission-line spectra, that are characterized by the presence of strong hydrogen lines and by the absence or weak presence of forbidden lines of lowly-ionized metals (e.g. [O III] $\lambda 4959$, $\lambda 5007$, [N II] $\lambda 6584$), hence the name *Balmer-dominated shocks*. The seminal paper of Chevalier et al. (1980) established several important results in the understanding of the emission mechanisms of BDSs. The H α , H β and H γ lines of Tycho's SNR, reported by Chevalier and coworkers, show a profile that will be observed later in many other faint shock filaments around SNRs and consists of the superposition of two components, a narrow component with typical full-width at half-maximum (FWHM) values of $\sim 10 \text{ km s}^{-1}$ and a broad component with typical FWHM of $\sim 1000 \text{ km s}^{-1}$. The two components are explained in the description of BDSs as non-radiative collisionless shocks. The main assumption to interpret the two component spectra is that the SNR shock wave is moving into a partially neutral interstellar medium. This requires that the neutral gas is able to survive the ionizing radiation emitted by the SNR. Just to give an example, in the particular case of Tycho's remnant, Chevalier & Raymond (1978) find that the time required to ionize a hydrogen atom at the edge of the remnant is approximately $2.5 \cdot 10^4$ years. Because this is long compared with the 400-year age of the remnant, the blast wave can interact directly with neutral atoms. We also assume that all neutral hydrogen atoms interacting with the protons and the electrons are at the ground level 1s. In fact, let v_s be the shock velocity and $\sigma_{coll} \approx 10^{-15} \text{ cm}^2$ the collisional de-excitation cross-section by protons and electrons, the collisional deexcitation can be neglected because it occurs on a typical time scale $\tau_{coll} = (n_i \sigma_{coll} v_s)^{-1} \approx 10^7 \text{ s}$ (for $n_i = 1 \text{ cm}^{-3}$ and $v_s = 1000 \text{ km s}^{-1}$) which is much longer than spontaneous de-excitation, whose timescale (from upper state n to lower state m) is of the order:

$$\tau = \hbar / \Delta E \approx \frac{6.582 \cdot 10^{-16} \text{ eV} \cdot \text{s}}{13.6 (m^{-2} - n^{-2}) \text{ eV}} \approx \frac{4.8 \cdot 10^{-17}}{(m^{-2} - n^{-2})} \text{ s} \quad (1)$$

Hence, atoms decay to the ground state before undergoing any further collision. Let's now track the fate of every hydrogen atom that crosses the shock front and contributes to the formation of the H α or H β line. The situation is schematized in Fig. 2. As the hydrogen atom crosses the shock front, it can be (1) excited by an electron or a proton to the n -state level. The subsequent radiative cascade can lead to the $n=3$ or $n=4$ state, from which another radiative decay to the $n=2$ state represents the main contribution to the narrow component of the H α and H β line, respectively. Another possibility is that the hydrogen atom is (2) ionized by a proton or an electron. Radiative recombination can lead to the formation of a hydrogen atom at the n -state level. The subsequent radiative cascade can lead to the $n=3$ or $n=4$ state, from which another radiative decay to the $n=2$ state contributes to the narrow component of the H α and H β line, respectively. However, the contribution of recombination should be much smaller than collisional excitation by protons or electrons, since the SNR is non-radiative. The last possibility is the (3) charge exchange between a post-shock proton and the ground-state hydrogen. This

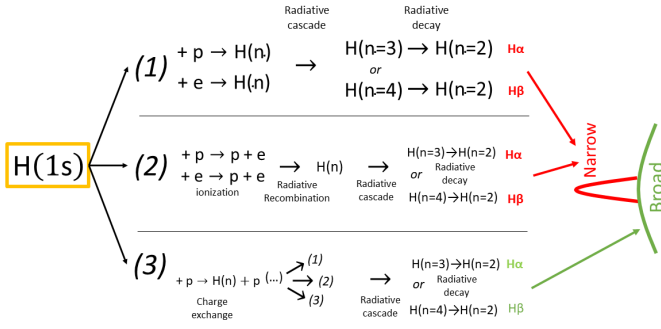


Fig. 2. A schematic representation of the theoretical $H\alpha$ and $H\beta$ emission model. Case 1 describes excitation, Case 2 ionization and Case 3 Charge-exchange contributions.

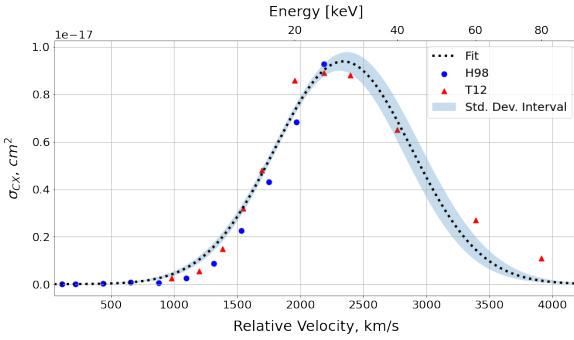


Fig. 3. H98 (blue dots) and T12 (red dots) CE cross-section for the reaction $p + H(1s) = H(3s) + p$. Black dotted line is the Gaussian fit to the two sets of data and the blue band describes the related standard deviation error.

lead to the formation of a fast ground-state hydrogen or a fast n -state excited hydrogen, that can reenter in reaction tree (1), (2) or (3). This time the radiative decay from $n=3$ or $n=4$ to $n=2$ represents a contribution to the broad component of the $H\alpha$ and $H\beta$ line, respectively. In order to simplify the model, it can be neglected the cascade contributions to the $H\alpha$ and $H\beta$ line formation from levels higher than $n=3$ and $n=4$, respectively. They represent an effect $< 5\%$, as shown by Heng & Sunyaev (2008). It is neglected also the contribution to $H\alpha$ and $H\beta$ of ground-state hydrogen atoms, formed after a CE interaction, which are subsequently excited or ionized by protons and electrons. Under these assumptions, the broad component profile of the $H\alpha$ and $H\beta$ lines represents the velocity distribution of the post-shock protons that, after a CE reaction, form directly a fast excited hydrogen atom in the $n=3$ or $n=4$ state. The ratio of the intrinsic (unaffected by extinction, indicated by the subscript *int*) number of photons $(N_{H\alpha}/N_{H\beta})_{int}^b$ that contribute to the $H\alpha$ and $H\beta$ broad components (indicated by the superscript *b*) can be evaluated as the ratio of the CE cross-sections σ that populate the $n=3$ and $n=4$ state levels, weighted by the appropriate branching ratio factor (Tseliakhovich et al. 2012).

$$\left(\frac{N_{H\alpha}}{N_{H\beta}}\right)_{int}^b = \frac{\sigma(3s) + B_{3p,2s}\sigma(3p) + \sigma(3d)}{B_{4s,2p}\sigma(4s) + B_{4p,2s}\sigma(4p) + B_{4d,2p}\sigma(4d)} \quad (2)$$

2.3. Evaluation of the Charge Exchange cross-sections

A critical point to solve Eq. 2 is the knowledge of the CE cross-section for the fundamental reaction: $p + H(1s) = H(n\ell) + p$.

Many authors have theoretically evaluated this cross-section in different energy ranges. For example, in the low energy regime, in particular from 62.5 eV to 25 keV, Harel et al. (1998), hereafter H98, numerically solve the Schrodinger equation using a molecular treatment of the atomic collision, obtaining reliable CE cross-sections for the hydrogen atom in the final state $n = 1, 2, 3, 4$. The same is obtained in a higher energy range, between 5 and 80 keV, by Tseliakhovich et al. (2012), hereafter T12, who implement a faster and improved algorithm, which directly solves the Schrodinger equation with variable resolution and utilizes a hybrid spatial-Fourier grid. Comparing the two results we can evaluate the CE cross-section over a wide velocity range, as shown as an example in Fig. 3 for the transition $p + H(1s) = H(3s) + p$. CE cross-section in cm^2 spans the relative proton-hydrogen velocity from ~ 500 to 4000 km s^{-1} . Blue dots are the tabulated points from H98 (see Tab. 1 of H98), red upward triangles are the tabulated points from T12 (see Tab. 4 of T12) and the black dotted line with the blue band is a Gaussian fit to the two sets of data with the related standard deviation error. It can be noticed that the values from the two research teams overlap quite well within the velocity range in common with the two sets of data. Such a fit has been considered for all the transitions up to the one with the hydrogen atom in the final state $n = 4$. The calculation of expression 2 as a function of the relative proton-hydrogen velocity using CE cross-section fitted with the available data is shown in Fig. 4 for the case A (red) and B (green). These are compared with the blue solid line which defines the standard radiative recombination $H\alpha/H\beta$ decrement.

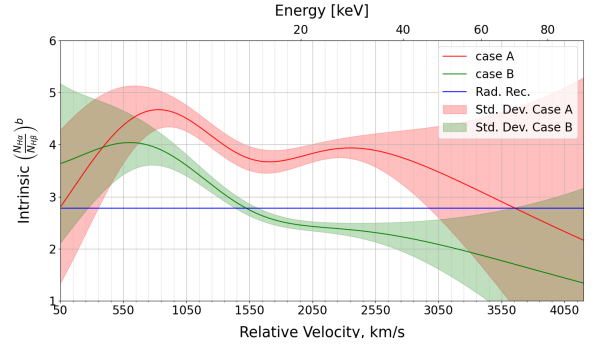


Fig. 4. Ratio of the intrinsic (unaffected by extinction, indicated by the subscript *int*) number of photons $(N_{H\alpha}/N_{H\beta})_{int}^b$ that contribute to the $H\alpha$ and $H\beta$ broad components (indicated by the superscript *b*). The red and green solid lines refer respectively to case A (the emitting region is optically thin in all H I absorption lines) and case B (the emitting region is optically thick in the Lyman lines). The red and green stripes represent the standard deviation. The blue solid line is the standard radiative recombination $H\alpha/H\beta$ decrement.

3. Spectroscopic observations on the SNR RCW 86

3.1. The SNR RCW 86

The filamentary emission nebula RCW 86 (also known as ESO 134-11), discovered by Rodgers et al. (1960), has coordinates RA: 14:40:29 DEC: -62:38:4, epoch=J2000 (Lauberts 1982). RCW 86 is frequently cross-identified with SNR G315.4-02.3, also known as MSH 14-6-03 (Mills et al. 1960), that has a diameter of about $40'$ and the centre at coordinates RA: 14:43:00.0 DEC: -62:30:00 (Green 2014). The optical spectrum of the filaments obtained by Westerlund & Mathewson (1966) shows strong emission lines of [S II] $\lambda 6717$, $\lambda 6731$, a characteristic fea-

ture of supernova remnants. It has been suggested that RCW 86 is the remnant of the supernova explosion that occurred in the year 185 A.D. (e.g. Clark & Stephenson 1977). This explosion is registered in the catalogue by Tse-Tsung (1957) of ancient astronomical events. However, this is not universally accepted (e.g. Rosado et al. 1996). Further optical emission spectra, that cover the blue from 3700 Å to 5100 Å and the red from 5800 Å to 7200 Å in six different filaments of RCW 86 were obtained by Ruiz (1981). Leibowitz & Danziger (1983) identify many of the brightest RCW 86 filaments, characterized by forbidden lines from a wide range of ionization species, including [O II], [O III], [N II], and [S II], which have strengths comparable to that of $H\alpha$ and $H\beta$ one. Sollerman et al. (2003) report high-resolution spectra of the founding $H\alpha$ profiles consisting just of a narrow component with a full-width half maximum (FWHM) of 30/40 km s⁻¹. However, RCW 86 has also faint filaments, where the forbidden lines are very weak or entirely absent. Long & Blair (1990) investigated the spectra of these Balmer-dominated filaments in the wavelength range 6250-7450 Å, obtaining the characteristic $H\alpha$ profile with a broad component and a narrow component. Smith (1997), using the UM/CTIO Curtis Schmidt telescope, reports the discovery of Balmer-dominated filaments along almost the complete periphery of RCW 86. The measurement of the FWHM of the broad $H\alpha$ component of the southwestern part of RCW 86, taken by Ghavamian et al. (2001), turned out to be 562 ± 18 km s⁻¹. Helder et al. (2009) use Chandra X-ray proper motion measurements to measure a shock velocity of $v_s = 6000 \pm 2800$ km s⁻¹ for northeastern RCW 86 filament, whose spectrum is reported in Fig. 5. The distance to RCW 86 was evaluated by Westerlund (1969), who found a value of 2.5 kpc using an OB association. Matsunaga et al. (2001) found a distance of 2.5 kpc for the molecular supershell seen in CO emission in the same direction of RCW 86, whose line-of-sight velocity agrees with that of RCW 86. However, in another work, Bocchino et al. (2000) derive a distance for RCW 86 of 1.18 kpc using the Sedov model in conjunction with the X-ray emission of the Northern filament. In further calculations, we consider a distance towards RCW 86 to be a mean value of those estimated, which is 1.84 kpc.

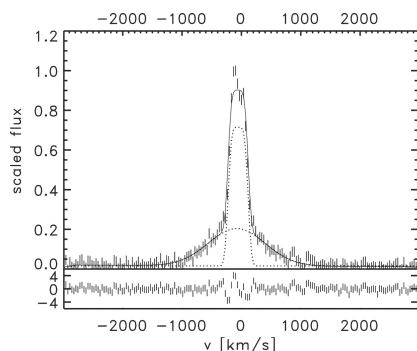


Fig. 5. The $H\alpha$ spectrum of the SNR RCW 86 observed by Helder et al. (2009). The dotted lines are the broad component and the narrow component. The best-fitting spectrum is overplotted. The lower panel shows the residuals divided by the errors.

3.2. Observations and data reduction

RCW 86 optical spectra were acquired in 2007 and 2018 with the FORS2 instrument installed on the 8-m telescope UT1 (Antu) of the Very Large Telescope (VLT) (Appenzeller et al. 1998). We used two sets of observations, each of them pointing toward two

different RCW 86's non-radiative filaments, which from now on we refer to as filament N (North) and SW (South West), according to their position in the remnant. Spectra of the filament N cover the wavelength range of the $H\alpha$ line while those of the filament SW cover the wavelength range of the $H\beta$ line. Fig. 6

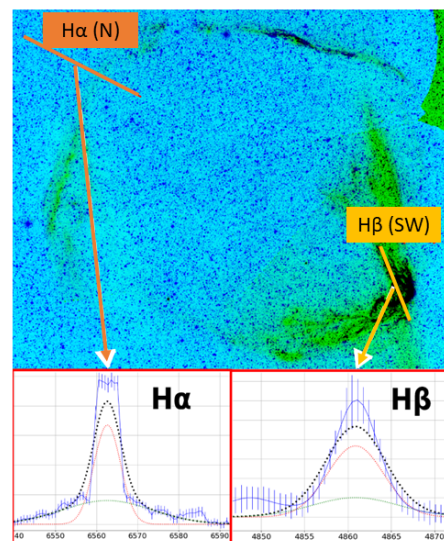


Fig. 6. Upper panel is a composition of images of RCW 86 in different bands. Green indicates the 0.2-10 keV X-ray band from the XMM-Newton space telescope. Blue indicates the $H\alpha$ optical band from SuperCOSMOS H-alpha Survey (SHS). The two locations of the slits used to get the optical spectrum in the two filaments N and SW are indicated respectively with orange and yellow lines. In the lower panels are shown the $H\alpha$ spectrum (right), corresponding to the position N and the $H\beta$ spectrum (left), corresponding to the position SW.

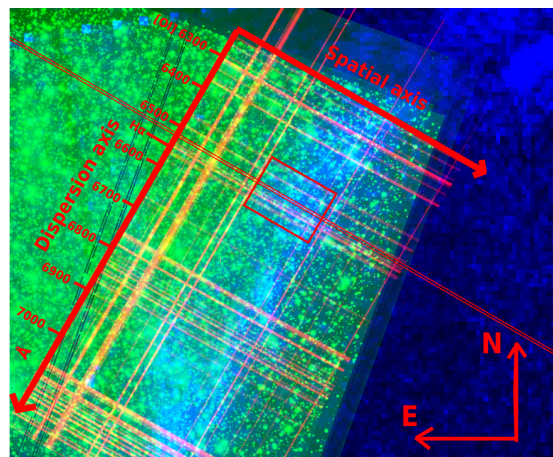


Fig. 7. Image shows how to perform the identification procedure of filament N. Note the presence of telluric spectral lines crowding the CCD image, easily recognizable by their presence along the entire spatial direction.

shows a composition of images of RCW 86 in different bands. Green is the 0.2-10 keV X-ray band from the XMM-Newton space telescope. Blue is the $H\alpha$ optical band from SuperCOSMOS H-alpha Survey (SHS). Images cover a box of 40 arcminutes centred at RA 14:43:00.00, DEC -62:30:00.0, which is the centre of SNR in radio band (Green 2014). The two locations of the slits used to get the optical spectrum in the two filaments N and SW are indicated respectively with orange and yellow lines. Comparing the spectrum and the associated images data

is possible to identify along the slit the regions corresponding to the SNR filament. This is shown, as an example for the filament N, in Fig. 7. Blue is the 0.2-10 keV X-ray band from the XMM-Newton space telescope. Green is a montage of the optical images associated with the spectrum. Red is the raw spectrum, overlotted so that the coordinates along the spatial axis coincide with those of the underlying images. The location of the slit used to get the optical spectrum in the filament is shown with a red thin region. The thick red box region is where the shock, visible in the X-ray band, crosses the slit. The flux-calibrated 2d

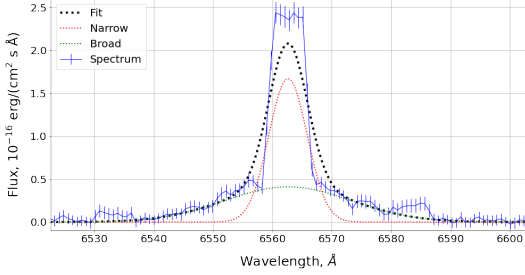


Fig. 8. Image shows the H α observed spectrum (blue solid line), the resulting two-component Gaussian fit (black dotted line) and the associated narrow (dotted red) component and broad (dotted green) component.

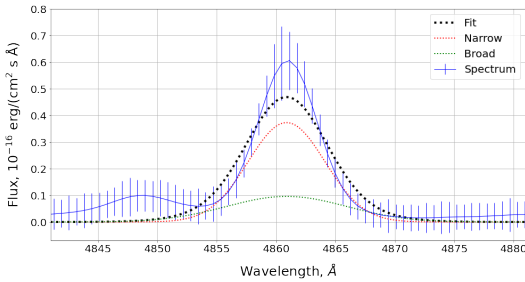


Fig. 9. Image shows the H β observed spectrum (blue solid line), the resulting two-component Gaussian fit (black dotted line) and the associated narrow (dotted red) component and broad (dotted green) component.

spectrum with wavelength rectified and calibrated was obtained using the ESO Reflex data reduction pipeline. The subtraction of the background, fitted with a second-degree Chebyshev polynomial and the subsequent spectra extraction were performed using the IRAF/IRAF packages¹. H α and H β spectra were obtained in "Longslit Spectroscopy (LSS)" mode, using a slit with a width of 2.5" and 1.0", respectively. In order to operate on the two spectra we convolved the H β spectrum with a Gaussian function with the same resolution as the H α spectrum. Fig. 8 and Fig. 9 show respectively the resultant H α and H β observed spectrum (blue solid line) as well as the resulting two-component Gaussian fit (black dotted line) with the associated narrow (dotted red line) component and broad (dotted green line) component.

4. Results

In order to compare the calculated $N_{H\alpha}/N_{H\beta}$ ratio with the observed ones, we have to take into account how the interstellar

¹ IRAF is distributed by the National Optical Astronomy Observatory, which is operated by the Association of Universities for Research in Astronomy, Inc.

extinction can affect the observed H α and H β flux and resume the intrinsic emissions from the observed ones. Let I be the intrinsic (unaffected by extinction, indicated by the subscript *int*) or observed (subscript *obs*) ratio of the number of photons N that contribute to the H α and H β broad (superscript *b*) component or narrow (superscript *n*) component.

$$I_{int(obs)}^{b(n)} = \left(\frac{N_{H\alpha}}{N_{H\beta}} \right)_{int(obs)}^{b(n)}$$

Let R be the intrinsic or observed ratio of the H α flux $F_{H\alpha}$ and H β flux $F_{H\beta}$ for the broad component or the narrow component.

$$R_{int(obs)}^{b(n)} = \left(\frac{F_{H\alpha}}{F_{H\beta}} \right)_{int(obs)}^{b(n)} = \left(\frac{N_{H\alpha} h \nu_{H\alpha}}{N_{H\beta} h \nu_{H\beta}} \right)_{int(obs)}^{b(n)} = 0.74 \cdot I_{int(obs)}^{b(n)}$$

where h is the Planck constant and $\nu_{H\alpha}$, $\nu_{H\beta}$ are respectively the H α and H β frequencies in vacuum. The narrow collisional component I_{int}^n can be evaluated from Tab. 1 of Chevalier & Raymond (1978), which lists the number of photons produced during the ionization of a plasma that is in the typical conditions present in supernova remnants. From this, we have that

$$I_{int}^n = \begin{cases} 0.048/0.016 = 3 & \text{Case A} \\ 0.27/0.075 = 3.6 & \text{Case B} \end{cases} \quad (3)$$

We need to correct this range for the interstellar extinction, that in the Johnson UBV photometric system is taken into account through the colour excess E_{B-V} defined as:

$$E_{B-V} = (B - V)_{obs} - (B - V)_{int} \quad (4)$$

where $(B - V)_{int}$ and $(B - V)_{obs}$ are respectively the intrinsic and observed color indices. In a SNR, we can use the approximation that the emission of H α and H β (in its broad component or narrow component) is the only significant contribution to the V and B passband, respectively. This means that

$$(B - V)_{int(obs)} = -2.5 \log \left(1/R_{int(obs)}^{b(n)} \right) \quad (5)$$

Substituting Eq. 5 in Eq. 4

$$2.5 \log \left(1/R_{int}^n \right) - 2.5 \log \left(1/R_{obs}^n \right) = E_{B-V} \quad (6)$$

The mean ratio of extinction in the visual passband A_V to path-length is 1.8 mag kpc^{-1} and tends to increase linearly for a line of sight close to the plane of the Milky Way and distances up to a few kiloparsecs from the Sun. Therefore, we can use this value for RCW 86, which is very close to the galactic plane (galactic coordinates in the J2000 epoch are ℓ : 315.4168, b : -02.3639) and has a distance of 1.84 kpc. In the Johnson system, the extinction in the visual passband may be related to E_{B-V} by $A_V = R_V \cdot E_{B-V}$ where R_V is termed the ratio of total to selective visual extinction. Theoretically, R_V is expected to depend on the composition and size distribution of the grains. However, in the low-density ISM, R_V has been shown to be virtually constant and a value of $R_V \approx 3.05 \pm 0.15$ may be assumed for most lines of sight (Whittet 2002). This leads to

$$\frac{R_{obs}^n}{R_{int}^n} = \frac{0.74 \cdot I_{obs}^n}{0.74 \cdot I_{int}^n} = 10^{(0.59 \cdot d)/2.5} \approx 2.72 \quad (7)$$

where d is the distance of RCW 86 in kpc and the last equality is for a distance of 1.84 kpc. Therefore, from Eq. 3 the expected observed range is

$$I_{obs}^n = 2.72 \cdot I_{int}^n = \begin{cases} 8.16 & \text{Case A} \\ 9.79 & \text{Case B} \end{cases} \quad (8)$$

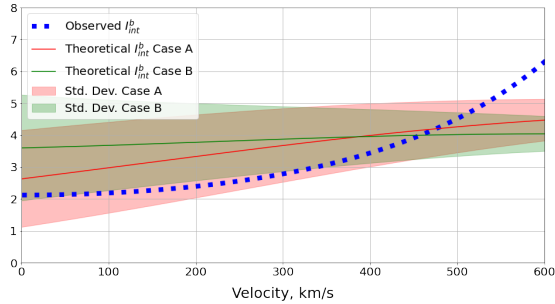


Fig. 10. Blue dotted line is the experimental ratio I_{int}^b . The solid lines are the theoretical I_{int}^b . Red refers to case A (the emitting region is optically thin in all H I absorption lines) and green to case B (the emitting region is optically thick in the Lyman lines). The red and green stripe represents the standard deviation error, which derives from the standard deviation errors in the parameters of the fit of the CE cross-sections.

R_{obs}^b is obtained by dividing the profile of the broad component resulting from the fit of $H\alpha$ and $H\beta$ and converted into the number of photons I_{int}^b after having corrected for the reddening. Fig. 10 compares the I_{int}^b (blue dotted line) with the theoretical one obtained, in Section 2, from the CE cross-section atomic data, weighed with the appropriate branching ratio (Fig. 4). In particular, the red and the green solid lines are the theoretical ratio I_{int}^b respectively for the case A (the emitting region is optically thin in all H I absorption lines) and the case B (the emitting region is optically thick in the Lyman lines), while the red and green stripes represent the standard deviation error. As it can be noticed, the I_{int}^b values obtained from the observed spectra are in good agreement with Case A of CE. This clearly indicates that the $H\alpha/H\beta$ spectroscopic indicator can be used to detect the CE phenomenon and therefore the presence of shocks in our Galaxy from which cosmic rays are accelerated.

4.1. Photometric Charge-Exchange indicator

Since large-field spectroscopic surveys of diffuse clouds are still a long way off, our method based, on a spectroscopic indicator, cannot be used for a mapping of LECRs in the whole Galaxy until the advent of new facilities such as THE wide-field spectroscopic telescope (WST) Bacon et al. (2023), which will not be operational until 2035. In view of the large photometric surveys that will instead start in the next years (such as LSST in 2025), we will investigate the possibility of deriving a photometric indicator, based on colour indices, from our spectroscopic indicator.

Fig. 11 shows the g (cyan), r (green) and i (yellow) LSST filter throughput with overplotted the $H\alpha$ and $H\beta$ central wavelengths, which respectively fall in the r and g filter. It is evident from this figure, that a variation in the spectroscopic $H\alpha/H\beta$ ratio due to CE should turn into a $g-r$ colour index variation too.

We will identify the best photometric indicator of Cosmic Ray passage by comparing different indicators such as $(g-r)$, $(r-i)$, $(g-r)-(r-i)$ in objects known as accelerators. With this aim, we have requested and obtained time for a deep VST imaging, in the filters g , r , i and $H\alpha$, covering 21 sq.deg area of the SCORPIO 150 sq.deg field, already observed by the Australian SKA Pathfinder (ASKAP) during the pilot phase of the EMU survey, where many SNRs and radio bright filaments have been detected.

We are working to define a photometric indicator that maximizes the signal-to-noise ratio (SN) for Balmer-dominated sources and which enables us to differentiate whether a neb-

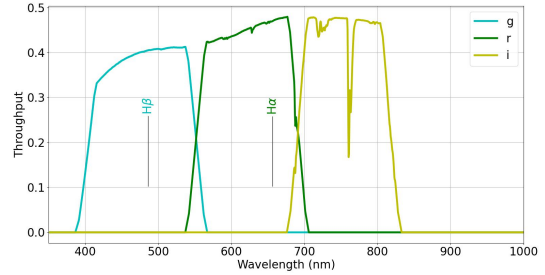


Fig. 11. LSST g , r and i filters, $H\alpha$ and $H\beta$ wavelength are indicated.

ula is affected by CE reactions or not. In this sense, our data are absolutely performant as they contain SNRs affected by CE and unaffected clouds. We will look for that indicator that maximises the percentage variation between the two types of clouds. Furthermore, The cross-match with radio synchrotron (from ASKAP maps) will give morphological and energetic information useful to refine the photometric indicator so that it could be applied to other CRs source candidates such as X and gamma-ray binaries, star formation regions, pulsar and pulsar wind nebula, superbubbles, flare, WR and LBV stars that LSST will observe in the next few years.

5. Conclusions

The emission model calculations developed in this work predicts that the $H\alpha/H\beta$ line profile ratio doubles when in the presence of CE reactions due to the enhanced broad components of the Balmer lines. This means that the spectroscopic ratio $H\alpha/H\beta$ can be used as an indicator of CE passage. We tested the indicator in the supernova remnant RCW 86 spectra and we find that the analysis of Balmer lines is in accordance with the expected values from the theoretical model, confirming both the CE nature of the Balmer-dominated filaments observed and the efficiency of the $H\alpha/H\beta$ spectroscopic indicator. Spectroscopic variations also have an impact on the photometric counterpart, leading us to investigate possible photometric indicators of CE reactions in the regions of interest. We are working on VST maps, with the purpose of identifying a photometric indicator which enables to differentiate whether a nebula is affected by CE reactions or not.

The photometric identification strategy, based on colour indices, would make the technique fast and particularly suitable to be applied to the large optical surveys that are planned for the next decades, such as LSST, whose enormous amount of data combined with the radio, X-ray and gamma counterparts could allow us, in the not-so-distant future, to obtain the first map of low-energy cosmic rays sources in our Galaxy.

Acknowledgements.

Appendix A: Einstein A-coefficients

In Tab. A.1 are summarized the Einstein A-coefficients from NIST Atomic Spectra Database (Kramida et al. 2021). These values were used in Section 2 to calculate the relevant branching ratio for the $H\alpha$ and $H\beta$ transition.

| Lower level Conf, Term, J | Upper level Conf, Term, J | A (s^{-1}) |
|------------------------------|------------------------------|----------------|
| $1s \ ^2S \ 1/2$ | $3p \ ^2P \ 1/2$ | 1.6725e+08 |
| $1s \ ^2S \ 1/2$ | $3p \ ^2P \ 3/2$ | 1.6725e+08 |
| $2s \ ^2S \ 1/2$ | $3p \ ^2P \ 1/2$ | 2.2449e+07 |
| $2s \ ^2S \ 1/2$ | $3p \ ^2P \ 3/2$ | 2.2448e+07 |
| $2p \ ^2P \ 1/2$ | $4s \ ^2S \ 1/2$ | 8.5941e+05 |
| $2p \ ^2P \ 3/2$ | $4s \ ^2S \ 1/2$ | 1.7190e+06 |
| $3p \ ^2P \ 1/2$ | $4s \ ^2S \ 1/2$ | 6.1182e+05 |
| $3p \ ^2P \ 3/2$ | $4s \ ^2S \ 1/2$ | 1.2238e+06 |
| $2p \ ^2P \ 1/2$ | $4d \ ^2D \ 3/2$ | 1.7188e+07 |
| $2p \ ^2P \ 3/2$ | $4d \ ^2D \ 3/2$ | 3.4375e+06 |
| $2p \ ^2P \ 3/2$ | $4d \ ^2D \ 5/2$ | 2.0625e+07 |
| $3p \ ^2P \ 1/2$ | $4d \ ^2D \ 3/2$ | 5.8647e+06 |
| $3p \ ^2P \ 3/2$ | $4d \ ^2D \ 3/2$ | 1.1729e+06 |
| $3p \ ^2P \ 3/2$ | $4d \ ^2D \ 5/2$ | 7.0376e+06 |
| $1s \ ^2S \ 1/2$ | $4p \ ^2P \ 1/2$ | 6.8186e+07 |
| $1s \ ^2S \ 1/2$ | $4p \ ^2P \ 3/2$ | 6.8186e+07 |
| $2s \ ^2S \ 1/2$ | $4p \ ^2P \ 1/2$ | 9.6683e+06 |
| $2s \ ^2S \ 1/2$ | $4p \ ^2P \ 3/2$ | 9.6680e+06 |
| $3s \ ^2S \ 1/2$ | $4p \ ^2P \ 1/2$ | 3.0652e+06 |
| $3s \ ^2S \ 1/2$ | $4p \ ^2P \ 3/2$ | 3.0650e+06 |
| $3d \ ^2D \ 3/2$ | $4p \ ^2P \ 3/2$ | 3.4754e+04 |
| $3d \ ^2D \ 3/2$ | $4p \ ^2P \ 1/2$ | 3.4759e+05 |
| $3d \ ^2D \ 5/2$ | $4p \ ^2P \ 3/2$ | 3.1280e+05 |

Table A.1. The first two columns show lower and upper energy level configuration, term and J values. The last column gives the Einstein A-coefficients for transitions involved between the two levels. The source is the NIST Atomic Spectra Database (Kramida et al. 2021).

References

- Appenzeller, I., Fricke, K., Fürtig, W., et al. 1998, *The Messenger*, 94, 1
- Bacon, R., Roth, M. M., Amico, P., & Hernandez, E. 2023, *Astronomische Nachrichten*, 344, e20230117
- Bocchino, F., Vink, J., Favata, F., Maggio, A., & Sciortino, S. 2000, *A&A*, 360, 671
- Chevalier, R. A., Kirshner, R. P., & Raymond, J. C. 1980, *ApJ*, 235, 186
- Chevalier, R. A. & Raymond, J. C. 1978, *ApJ*, 225, L27
- Clark, D. H. & Stephenson, F. R. 1977, *The historical supernovae* (Elsevier)
- Gabici, S. 2022, *A&A Rev.*, 30, 4
- Gabici, S., Evoli, C., Gaggero, D., et al. 2019, *International Journal of Modern Physics D*, 28, 1930022
- Ghavamian, P., Raymond, J., Smith, R. C., & Hartigan, P. 2001, *ApJ*, 547, 995
- Green, D. A. 2014, *Bulletin of the Astronomical Society of India*, 42, 47
- Harel, C., Jouin, H., & Pons, B. 1998, *Atomic Data and Nuclear Data Tables*, 68, 279
- Helder, E. A., Vink, J., Bassa, C. G., et al. 2009, *Science*, 325, 719
- Heng, K. 2010, *PASA*, 27, 23
- Heng, K. & Sunyaev, R. A. 2008, *A&A*, 481, 117
- Ivezic, Ž., Kahn, S. M., Tyson, J. A., et al. 2019, *ApJ*, 873, 111
- Kramida, A., Yu. Ralchenko, Reader, J., & and NIST ASD Team. 2021, *NIST Atomic Spectra Database* (ver. 5.9), [Online]. Available: <https://physics.nist.gov/asd> [2022, May 5]. National Institute of Standards and Technology, Gaithersburg, MD.
- Lauberts, A. 1982, *ESO/Uppsala survey of the ESO(B) atlas* (European Southern Observatory Garching)
- Leibowitz, E. M. & Danziger, I. J. 1983, *MNRAS*, 204, 273

- Long, K. S. & Blair, W. P. 1990, *ApJ*, 358, L13
- Matsunaga, K., Mizuno, N., Moriguchi, Y., et al. 2001, *PASJ*, 53, 1003
- Mills, B. Y., Slee, O. B., & Hill, E. R. 1960, *Australian Journal of Physics*, 13, 676
- Morlino, G., Bandiera, R., Blasi, P., & Amato, E. 2012, *ApJ*, 760, 137
- Murphy, R. P., Sasaki, M., Binns, W. R., et al. 2016, *ApJ*, 831, 148
- Rauch, B. F., Link, J. T., Lodders, K., et al. 2009, *ApJ*, 697, 2083
- Rodgers, A. W., Campbell, C. T., & Whiteoak, J. B. 1960, *MNRAS*, 121, 103
- Rosado, M., Ambrocio-Cruz, P., Le Coarer, E., & Marcellin, M. 1996, *A&A*, 315, 243
- Ruiz, M. T. 1981, *ApJ*, 243, 814
- Smith, R. C. 1997, *AJ*, 114, 2664
- Sollerman, J., Ghavamian, P., Lundqvist, P., & Smith, R. C. 2003, *A&A*, 407, 249
- Stone, E. C., Frandsen, A. M., Mewaldt, R. A., et al. 1998, *Space Sci. Rev.*, 86, 1
- Tatischeff, V., Raymond, J. C., Duprat, J., Gabici, S., & Recchia, S. 2021, *MNRAS*, 508, 1321
- Tse-Tsung, H. 1957, *Soviet Ast.*, 1, 161
- Tselikhovich, D., Hirata, C. M., & Heng, K. 2012, *MNRAS*, 422, 2357
- Westerlund, B. E. 1969, *AJ*, 74, 879
- Westerlund, B. E. & Mathewson, D. S. 1966, *MNRAS*, 131, 371
- Whittet, D. 2002, *Dust in the Galactic Environment*, 2nd Edition, Series in Astronomy and Astrophysics (Taylor & Francis)